ChemPubSoc Europe

DOI: 10.1002/slct.201900602

Chemistry SELECT Full Papers

Catalysis

Electrospinning Preparation and Formation Mechanism of $BiVO_4/\alpha$, β-Bi_2O_3 Nanofibers with Enhanced Photocatalytic Properties

Fan Yang,[a] Xiaojiao Yu,*[a, b] Binghua Yao,[a] Jie Zhang,[a] and Jv Li[a]

Herein, the $BiVO_4/\alpha$, β-Bi_2O_3 nanofibers with moderate amounts of $BiVO_4$ nanoparticles (1-5 wt%) were successfully fabricated by combining electrospinning and hydrothermal method. The microstructure and properties of the prepared samples were characterized by X-ray diffraction, X-ray photoelectron spectroscopy, fourier transform infrared spectrometer, scanning electron microscopy, transmission electron microscope, ultraviolet-visible diffuse reflection, and photocurrent measurement. The results show that $BiVO_4$ had a substantial effect on the formation of β-Bi_2O_3 and the structure of the nanofibers. From the photocatalytic test results, it can be inferred that the RhB degradation efficiencies of pure $BiVO_4$ and α-Bi_2O_3 were lower than those of the composites considered in this study. The samples with a $BiVO_4$ content of 3 wt% displayed the best photocatalytic activity for RhB (the degradation efficiency of RhB and Tc was 96.1% and 77.1%, respectively) compared to that of other samples considered in this study. The reactive species in the photocatalytic process were also studied, and it was found that the $O_2^{\bullet -}$ play a leading role in this process. In addition, the two-step formation mechanism and the carries transmission mechanism of the composite nanofibers were constructed. This work provides a valuable reference for future research and design of high-performance photocatalysts.

Introduction

At present, there are many ways to treat organic wastewater. Among these methods, photocatalysis is a promising approach and has attracted substantial attention due to its advantages, such as being nontoxic, low cost, and stable in addition to nonsecondary pollution.[1] Photocatalyst plays a key role in photocatalytic oxidation. Due to its unique performance, the crystal structure,[2] morphology,[3] synthetic methods[4] of Bi_2O_3 have attracted abroad attention, and efforts are underway to improve its properties. Moreover, the main crystal types of Bi_2O_3 are α, β, γ, δ and ω. The common types are α and β, where the band gap are 2.72 eV[5] and 2.27 eV,[6] respectively. Many researchers have paid substantial attention to α-Bi_2O_3, whereas there have been only a few reports on metastable β-Bi_2O_3 due to the difficulty of fabricating it.[7] It is well known that β-Bi_2O_3 has a lower band gap energy and high optical absorption in the visible-light region, so the photocatalytic activity of β-Bi_2O_3 is higher than that of α-Bi_2O_3. However, visible light can be absorbed by pure Bi_2O_3, and the recombination efficiency of photogenerated carries is high in the single catalyst,[8] and this limits the application and generalization of Bi_2O_3 in the field of photocatalysis. Therefore, many visible-light-driven photocatalysts consisting of Bi_2O_3 and the material with suitable band gaps, such as $FeVO_4$,[9] TiO_2,[10] BiOX,[11] $SrTiO_3$,[12] $NiFe_2O_4$,[13] $Au/FeVO_4$,[14] ZnO,[15] and $Bi_2S_3/Bi_2O_2CO_3$,[16] have been explored to solve this problem. In particular, some researchers have attached great importance to β-Bi_2O_3/α-Bi_2O_3 heterojunction photocatalyst. Hou et al.[17] reported that the photocatalytic activity of a β-Bi_2O_3/α-Bi_2O_3 heterojunction for the degradation of cationic RhB and anionic MO under visible-light irradiation is superior to that of β-Bi_2O_3 sheets, which is attributed to the efficient charge separation and transfer across the β-Bi_2O_3/α-Bi_2O_3 phase junction. In addition, $Bi_2O_3/BiVO_4$ has also been studied before.

$BiVO_4$ is a non-toxic and environmentally friendly photocatalyst. The band gap is 2.4 eV,[18] which leads to high absorption of visible light. Mao et al.[19] prepared the $Bi_2O_3/BiVO_4$ heterostructure nanorods using a solvent thermal method, and their photocatalytic properties were better than those of Bi_2O_3 and $BiVO_4$, which was attributed to the presence of a p-n heterojunction that reduces the recombination efficiency of electron-hole pairs. $Bi_2O_3/BiVO_4$ nanocomposites were fabricated via a homogeneous precipitation method with different surface dispersants by Li et al.[20] and they studied the effect of different surfactants on the morphology of the nanoparticles and the effect of the relative proportion between $BiVO_4$ and Bi_2O_3 on photocatalytic activity. The results show that the structure and morphology of the $BiVO_4$ varied using different surface dispersants and Bi_2O_3(50 wt%)/$BiVO_4$ displayed the best photocatalytic activity of the composition ratios. To the best of our knowledge, the preparation of $Bi_2O_3/BiVO_4$ nanofiber by electrostatic spinning, however, has not been reported.

[a] F. Yang, Prof. X. Yu, Prof. B. Yao, J. Zhang, J. Li
School of Science, Xi'an University of Technology, Xi'an 710048, China
[b] Prof. X. Yu
Material Corrosion and Protection Key Laboratory of Shaanxi Province, Xi'an 710048, China
Tel: +86-029-82066360
E-mail: yxjw@xaut.edu.cn

Supporting information for this article is available on the WWW under https://doi.org/10.1002/slct.201900602

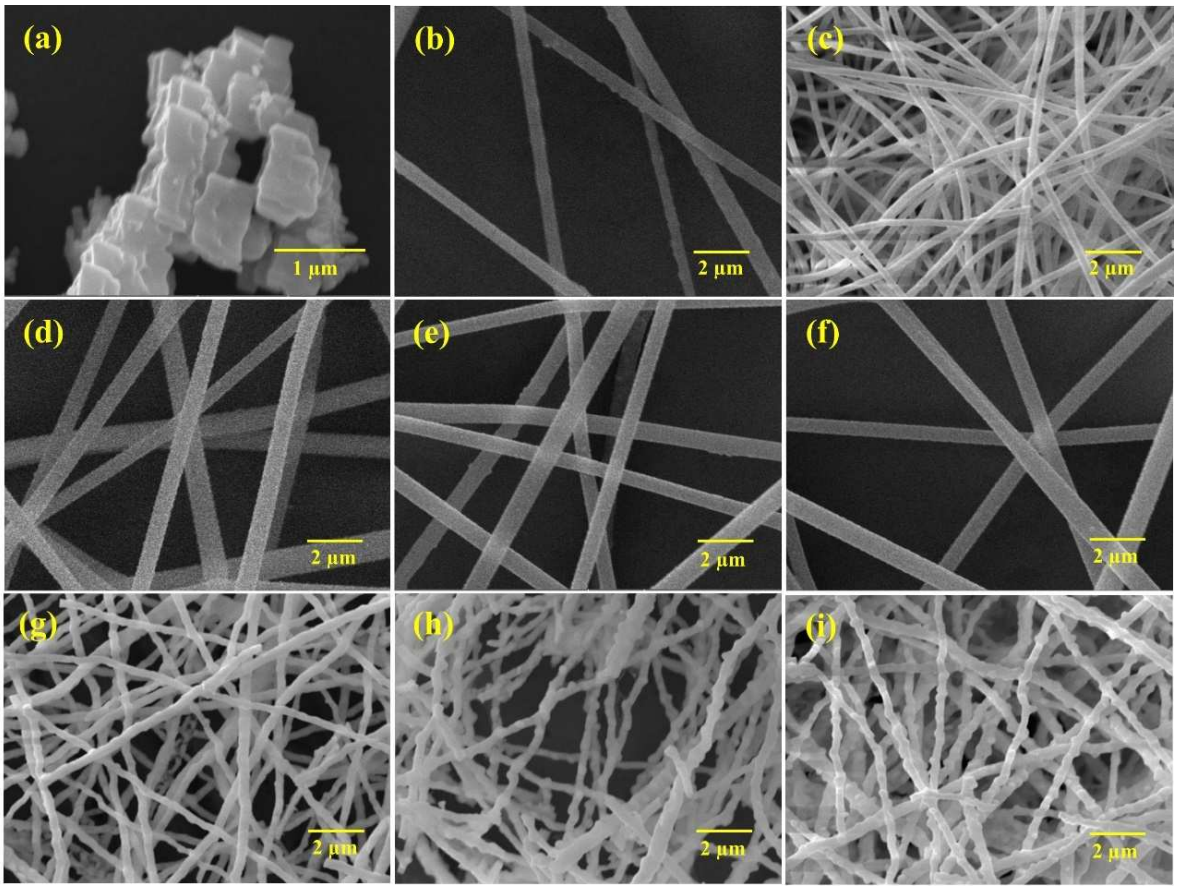

Figure 1. SEM of BV (a), BO-PVP (b), BO-BV0 (c), BO-BV1-PVP (d), BO-BV3-PVP (e), BO-BV5-PVP (f), BO-BV1 (g), BO-BV3 (h), and BO-BV5 (i)

To investigate their structure, composition and photocatalytic performance of nanofiber, we prepared $Bi_2O_3/BiVO_4$ nanofibers. The electrospinning solution was obtained by mixing the $BiVO_4$ powders acquired from the hydrothermal method and a solution that included bismuth sources and PVP, the electrospinning process was carried out subsequently. The $BiVO_4/\alpha$, β-Bi_2O_3 nanofibers were obtained after calcining of the $BiVO_4/Bi(NO_3)_3$/PVP nanofibers. RhB and Tc, as model pollutants, were used to measure the photocatalytic properties of the as-prepared samples. Finally, by combining the characterization results and related experiments, the two-step (heating and cooling) formation mechanism of the composite nanofibers was constructed. This work provided a valuable reference for the future research and designing of high-performance photocatalyst.

Results and discussion

SEM and TEM analyses

Figure 1 (a) shows the hydrothermal $BiVO_4$ nanoparticles. The images of the precursor fibers are displayed in Figure 1 (b) and (d)-(f), where it can be seen that the surfaces of all precursors are smooth. However, the diameter of BO-BVX-PVP (approximately 0.8 μm, X = 1, 3, 5) is larger than that of BO-PVP (approximately 0.6 μm). This may be attributed to the impact of $BiVO_4$ on the process of electrospinning; i.e., the addition of $BiVO_4$ leads to a variation in the stretching and separation of nanofibers. In addition, we found that $BiVO_4$ was wrapped in the precursor nanofibers from the TEM image of the BO-BV3-PVP precursor (Figure 2(a)). Calcined nanofibers are also observed in Figure 1(c) and (g)-(i). Compared with the precursor nanofibers, it is clear that all the nanofibers were attenuated after calcining because the organic template was removed. In

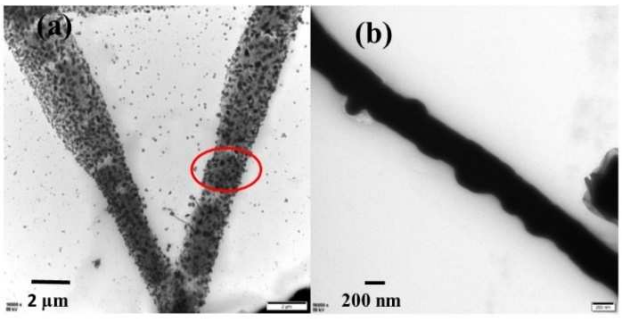

Figure 2. TEM of BO-BV3-PVP(a) and BO(b)

addition, as the content of $BiVO_4$ increased, the decoration on the surface of the nanofibers without calcining also increased, which may be beneficial for the photocatalytic process.

FTIR analysis

Figure 3 depicts the FTIR spectra of the samples in the wavenumber range from 400 cm^{-1} to 4000 cm^{-1}. The broad

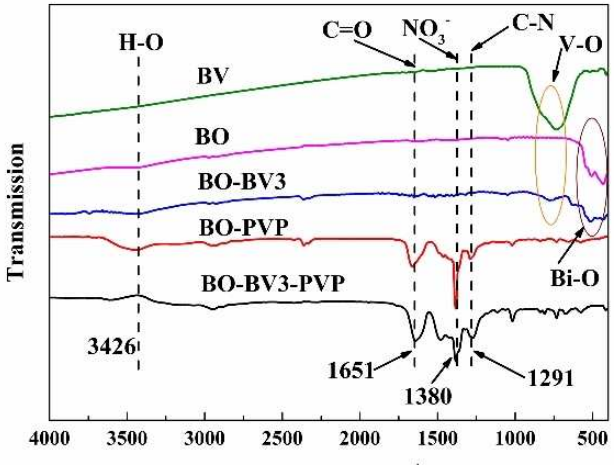

Figure 3. FTIR spectra of the BV, BO, BO-BV3, BO-PVP and BO-BV3-PVP

absorption at 3426 cm^{-1} was assigned to the O–H stretching vibration of the adsorbed water molecules. The bands at 1651 cm^{-1}, 1291 cm^{-1}, and 1380 cm^{-1} correspond to C=O and C–N in PVP[21] and NO_3^- in $Bi(NO_3)_3$, respectively. These bands disappeared after calcination. The results show that the organic template was removed and $Bi(NO_3)_3$ decomposed to Bi_2O_3. In addition, both the V–O stretching vibration located at 730–830 cm^{-1} and that of Bi–O located at 430–540 cm^{-1}[22] appeared in BO-BV3, which indicates that the nanofibers contained $BiVO_4$ and Bi_2O_3.

XPS analysis

XPS analysis was used to investigate the chemical composition and valence state of the samples.[23] The survey spectra of BO-BV3 (Figure 4) show the signals from Bi $4f_{7/2}$ and Bi$4f_{5/2}$ at approximately 156.6 eV and 162.0 eV, respectively, indicating that the bismuth ions in the composites are in a trivalent state.[24] The dominant peaks shown in Figure 4(c) at 529.4 eV, 531.2 eV and 532.8 eV are characteristic of structural oxygen (O 1*s*).[25] The peaks at 282.6 eV, 284.3 eV and 286.5 eV originated from the C 1*s* spectrum resulting from the decomposition of PVP.[26] The characteristic peaks of V 2*p* signals, however, are not observed in the pattern, which may show that the $BiVO_4$ was not present under the surface of the nanofibers.

XRD analysis

Figure 5(a) shows the XRD patterns of BV, BO, BO-BV1, BO-BV3, and BO-BV5. The diffraction peaks from BO and BV are in good accordance with the standard data of pure α-Bi_2O_3 (PDF#No.41-1449)[27] and monoclinic $BiVO_4$ (PDF#No.75-2480),[28] respectively. BO-BV1, BO-BV3, and BO-BV5, however, contain not only the peaks from α-Bi_2O_3 but also the peaks from β-Bi_2O_3 (PDF#No.78-1793),[29] and the sharpness of the diffraction peaks implies that all samples are highly crystallized and have no impurities.[30] Figure 5(b) shows the enlargement of Figure 5(a) from 25° to 30°. As the $BiVO_4$ content increased in the nanofibers, the intensity of the main diffraction peaks of α-Bi_2O_3 at 26.90° from the (111) plane, 27.93° from the (120) plane, and 28.01° from the (012) plane decreased, and the intensity of the main diffraction peak of β-Bi_2O_3 at 27.94° from the (201) plane increased, which indicates that increasing the amount of $BiVO_4$ that was added is beneficial for the formation of β-Bi_2O_3. In addition, the diffraction peaks of $BiVO_4$ in the $BiVO_4/\alpha$, β-Bi_2O_3 nanofibers did not appear because the amount of $BiVO_4$ is relatively low in the composites.[31]

Formation mechanism of $BiVO_4/\alpha$, β-Bi_2O_3 nanofibers

According to the results above, a possible growth mechanism for $BiVO_4/\alpha$, β-Bi_2O_3 nanofibers is proposed. The investigation of the mechanism shown in Figure 6 begins with a piece of fiber, and its process can be divided into two steps: the oxidation and decomposition of the precursor nanofibers (heating) and the crystal growth of Bi_2O_3 (cooling). During the heating process, the PVP template and $Bi(NO_3)_3$ are oxidized and decompose into gases and amorphous Bi_2O_3, respectively (a-b). After being held at temperature, the system cools to room temperature, and the crystals of α-Bi_2O_3 and β-Bi_2O_3 are formed at different times. It should be noted that β-Bi_2O_3 forms over the interface of $BiVO_4$ first (c), and α-Bi_2O_3 forms far away from the interface next (d).

To explain the interfacial crystallographic characteristics between two phases that are related by reproducible orientation relationships, Zhang et al.[32] proposed the edge-to-edge matching model. Combining this model and the results of the characterization above, we speculated that β-Bi_2O_3 and $BiVO_4$ are better matched than α-Bi_2O_3 and $BiVO_4$. Therefore, β-Bi_2O_3 was formed on the surface of $BiVO_4$ instead of α-Bi_2O_3 (e).

UV-Vis DRS analysis

Figure 7(a) shows the UV-Vis DRS spectra of the as-obtained samples. Compared with that of the pure α-Bi_2O_3, the light absorption of the composites is clearly expanded to the visible-light region. As shown in Figure 7(b), the band gap of BV, BO, BO-BV1, BO-BV3 and BO-BV5 can be calculated as follows according to Tauc's law: 2.45 eV, 2.74 eV, 2.41 eV, 2.40 eV and 2.42 eV, respectively, which indicates that photogenerated carriers can be produced by the $BiVO_4/\alpha$, β-Bi_2O_3 nanocomposite more easily than pure α-Bi_2O_3 and $BiVO_4$. Therefore, adding $BiVO_4$ appropriately can enhance the light utilization efficiency

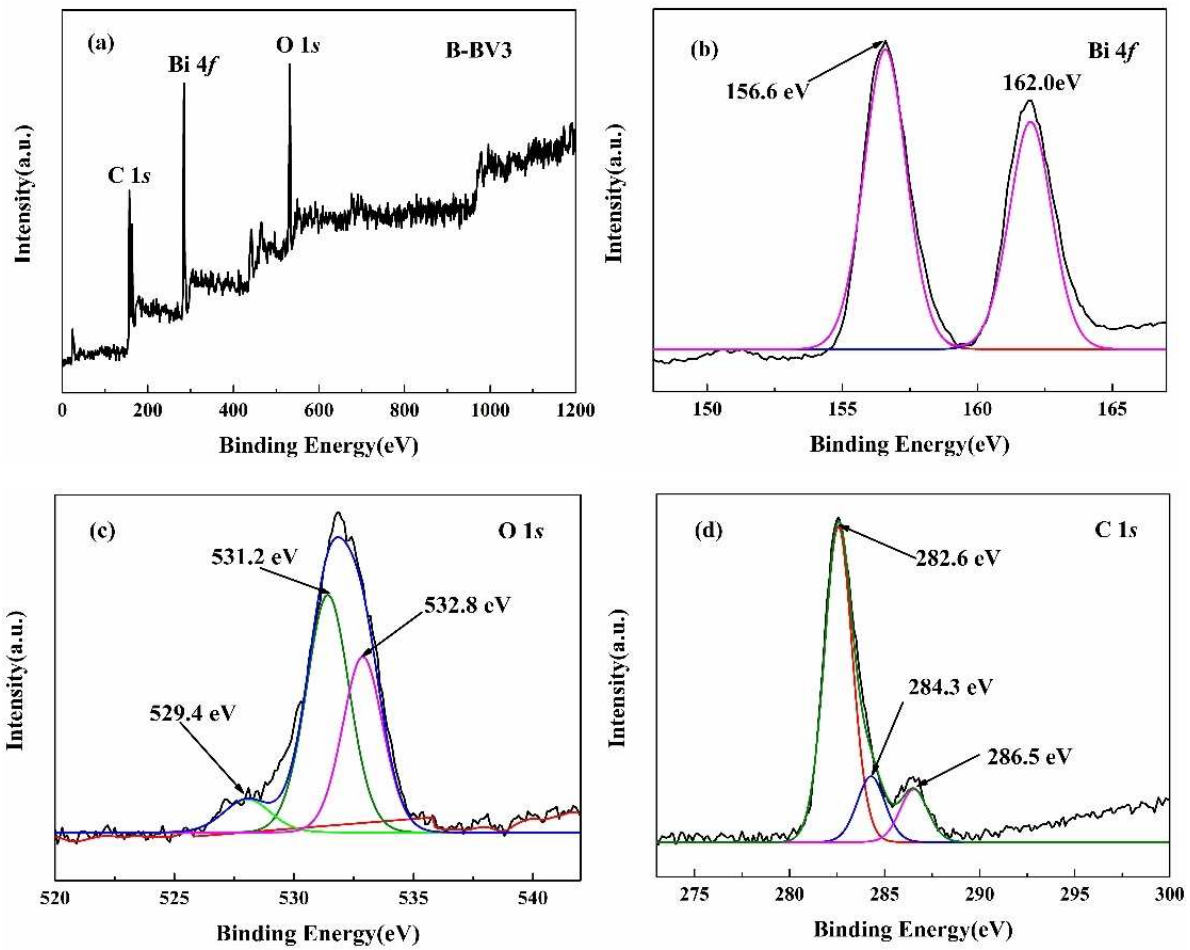

Figure 4. XPS patterns of BO-BV3

of $BiVO_4/\alpha$, β-Bi_2O_3 nanofibers, which can improve the photocatalytic activity of the samples.

Photocurrent test

The generation and transfer of the photogenerated carriers during the photocatalytic process can be evaluated by the photocurrent. Typically, the photocurrent is positively correlated with the separation efficiency of photogenerated electron holes. Figure 8 displays the photocurrent-time test curves of BV, BO, BO-BV1, BO-BV3, and BO-BV5 under visible light irradiation. Furthermore, compared to BV and BO, BO-BV3 exhibits a distinctly enhanced photocurrent response after one cycle (50 s). The results show that the photogenerated electron-hole pairs of BO-BV3 could be separated more effectively than those of the other samples.[33]

Photocatalytic properties and possible mechanism

To study the photocatalytic properties of the as-obtained nanocomposites for the degradation of organic pollutants, we carried out experiments involving the degradation of RhB. From the blank experiment (shown in Figure 9(a)), it was concluded that the self-photodegradation of RhB is negligible. The adsorption-desorption equilibrium of RhB in the dark can be established within 30 min. It can be inferred that the dark absorption of RhB and Tc, from Figure 9(c) and (d), are about 29% and 18%, respectively. The RhB degradation efficiencies of pure $BiVO_4$ and α-Bi_2O_3 are 65.6% and 70.5% within 110 min, respectively. With $BiVO_4$ added in, for one thing, the band gap of is narrow, which means it have a better optical absorption properties; for another thing, because the crystalline of sample will be changed from single (α-Bi_2O_3) to mixed phase (α-Bi_2O_3, β-Bi_2O_3, and $BiVO_4$), the separation rate of e^--h^+ pairs can be increased. And therefore, the $BiVO_4/\alpha$, β-Bi_2O_3 heterojunctions demonstrates a good photocatalytic activity to remove RhB. Typically, the highest degradation efficiency, 96.1%, can be reached by BO-BV3. Figure 9(b) displays the kinetic curves of RhB for the samples. We inferred that BO-BV3 follows polynomial rules, while the other samples follow first-order kinetic rules, and the half-life period of BO-BV3 is shorter than that of the others. Accordingly, the results indicate that the photocatalytic efficiency could be enhanced compared with that of the single samples when α-Bi_2O_3 is decorated with

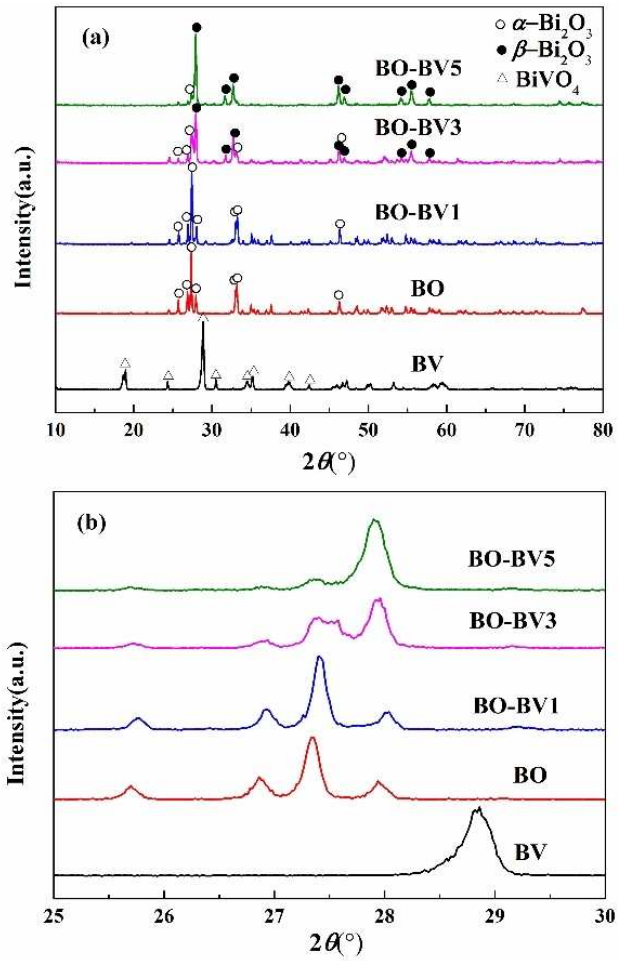

Figure 5. XRD patterns of BV, BO, BO-BV1, BO-BV3 and BO-BV5(a) and their enlarge figure(b)

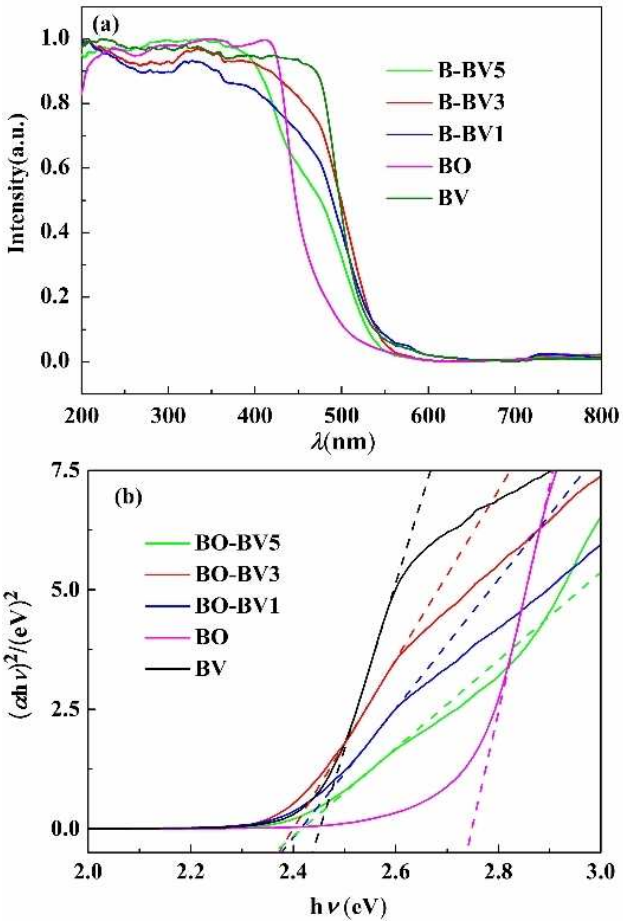

Figure 7. (a) UV-Vis DRS of samples with different content and (b) the plots of $(\alpha h\nu)^2$*vs* hν

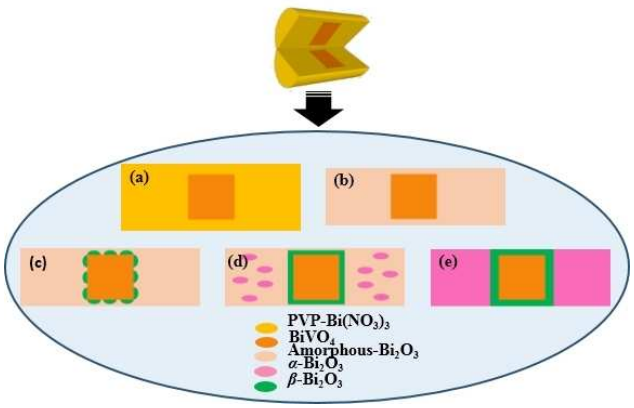

Figure 6. The sketch of formation mechanism of composites nanofibers

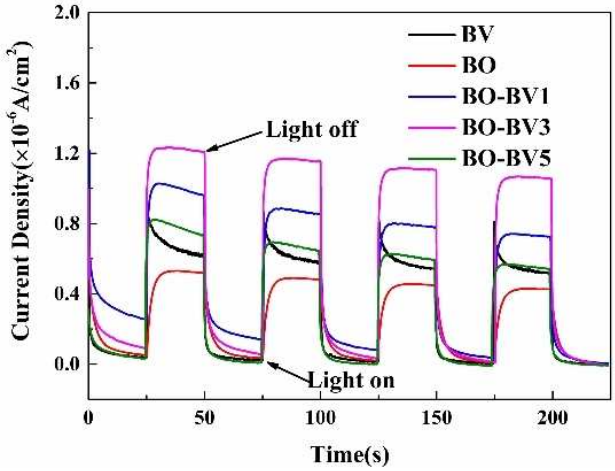

Figure 8. Transient photocurrent response of the samples

$BiVO_4$. Figure 9(c) shows the time-dependent absorption spectra of the RhB solution in the presence of BO-BV3 from 0 to 110 min. As the irradiation time increased, the maximum absorption band of RhB at 554 nm gradually decreased and eventually nearly disappeared after 110 min. Moreover, the blue shift of the main peak in the absorption curve was

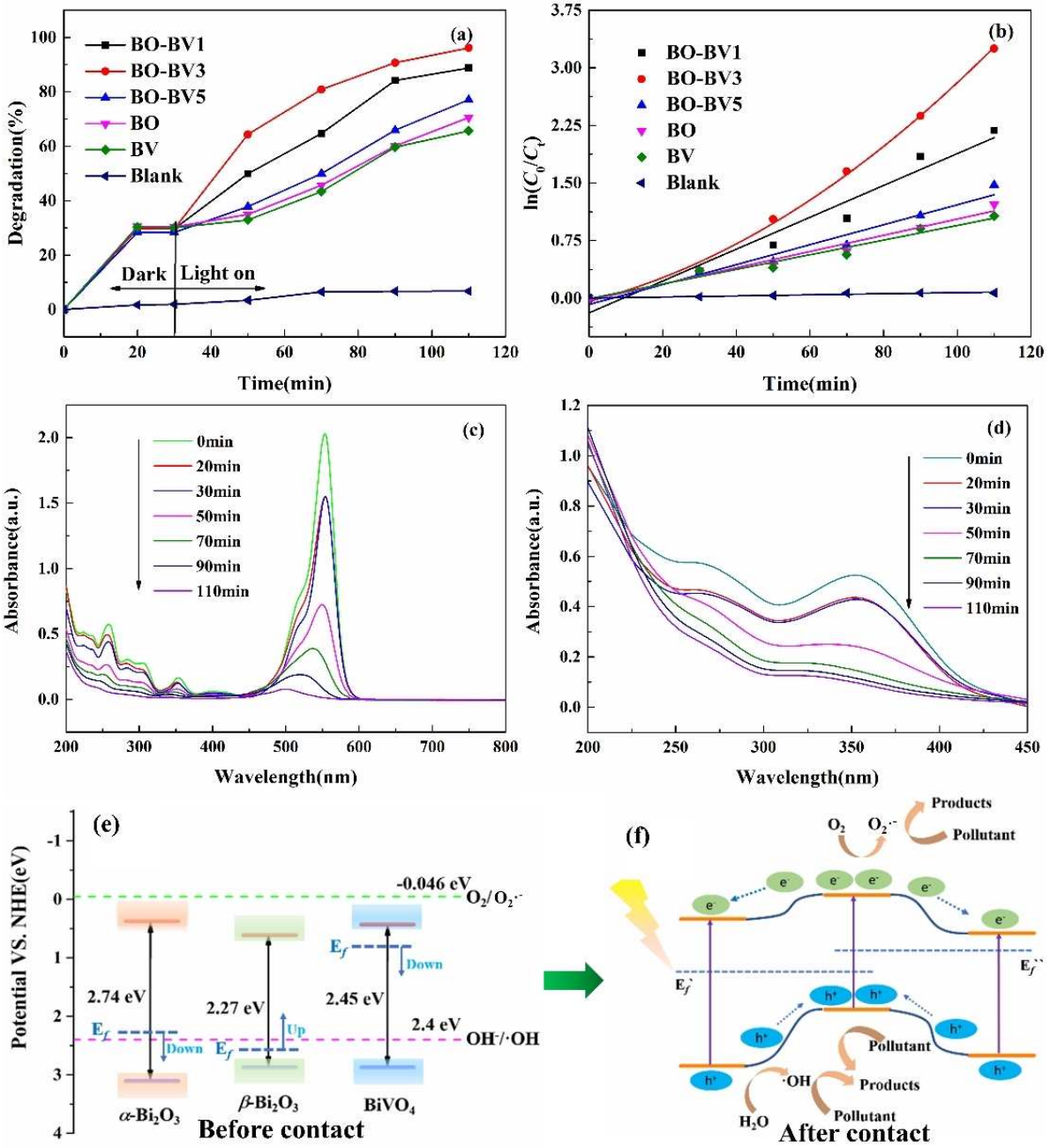

Figure 9. (a) Photodegradation profiles of RhB over samples, (b) the photocatalytic degradation kinetics curve of RhB, the evolution of the absorption spectra of RhB (c) and Tc (d) over time in the presence of samples, and (e)-(f) the mechanism of the photocatalytic reaction

attributed to the de-ethylation of the dye from N, N, N′, N′-tetra-ethylated rhodamine to rhodamine.[34] Removing Tc from water is a serious issue,[35] and the degradation of Tc by BO-BV3 was studied here. Figure 9(d) shows that BO-BV3 exhibits photocatalytic degradation activity (77.1%)

for Tc, which suggests that the photocatalyst possesses activity for its practical application. The possible mechanism was proposed to show the pathway of electron-holes transmission in the BO-BV3 and explain its enhanced photocatalytic performance (shown in Figure 9(e)-(f)). From the discussion mentioned above, the band gap of α-Bi_2O_3, β-Bi_2O_3 and $BiVO_4$ are 2.74 eV, 2.27 eV, and 2.45 eV, respectively. Through the following equations (1-2), the potentials of conductor band (CB) and the valence band (VB) can be obtained.

$$E_{VB} = X - E^e + 0.5Eg \quad (1)$$

$$E_{CB} = E_{VB} - Eg \quad (2)$$

Where X is the electronegativity (Bi_2O_3: 6.24 eV, $BiVO_4$: 6.16 eV) of the semiconductor; E^e is the energy of free electrons on the hydrogen scale (about 4.5 eV); Eg, E_{CB}, and E_{VB} are the band gap energy, CB potential, and VB potential of semiconductor. It can be found that the potentials (α-Bi_2O_3 for 0.37 eV, β-Bi_2O_3 for 0.61 eV, and $BiVO_4$ for 0.43 eV) are more positive than the standard reduction potential of $O_2/O_2\bullet^-$ (-0.046 eV), which means O_2 cannot be reduced to $O_2\bullet^-$, before they contact with each other (Figure 9(e)). However, when α-Bi_2O_3, β-Bi_2O_3, and $BiVO_4$ contact, the Fermi energy (E_f) will be changed to a balanced condition[36] (Figure 9(f)). As a result, the band of α-Bi_2O_3 and $BiVO_4$ are shifted downwards and while the band gap of β-Bi_2O_3 is shifted upwards to level that O_2 can be reduced to $O_2\bullet^-$. In addition, •OH, another reactive specie, is produced both in contact and not contact.

In the process of photocatalytic degradation, reactive species, such as electrons (e^-), superoxide radicals ($O_2\bullet^-$), valence band holes (h^+), and hydroxyl radicals (•OH), make a substantial difference.[37] The roles of these reactive species can be estimated by investigating the effects of scavengers of reactive species on photocatalytic degradation.[38] BO-BV3 was selected as the model photocatalyst to determine the relative importance of reactive species in the degradation of RhB. The results are shown in Figure 10. With the addition of BQ, the degradation rate of RhB was clearly decreased. The addition of BQ restrains the photocatalytic degradation process. Therefore, $O_2\bullet^-$ radicals played a key role in the degradation process. After EDTA and TBA were added to the reaction system, the rates for RhB degradation over BO-BV3 were 69.8% and 74.4%, respectively. These results indicate that h^+ and •OH also play an important role in the degradation process (after $O_2\bullet^-$). The possible reactions occurring in the photocatalytic process are given in Eqs. (3-9). When the light was turned on, the e^-- h^+ pairs were generated on the surface of the samples (Eq. (3)). Thereafter, e^- reacted with O_2 to form $O_2\bullet^-$ (Eq. (4)). The holes with strong oxidizing properties degrade RhB directly, and a portion of the holes might react with H_2O to form •OH (Eq. (5)), which can also be used to oxidize RhB. Some $O_2\bullet^-$ could degrade RhB, whereas some may form •OH (Eqs. (6)-(9)). As a result of the issues outlined above, the order of importance of the main active species in the system was deduced to be as follows: $O_2\bullet^- > h^+ >$ •OH.

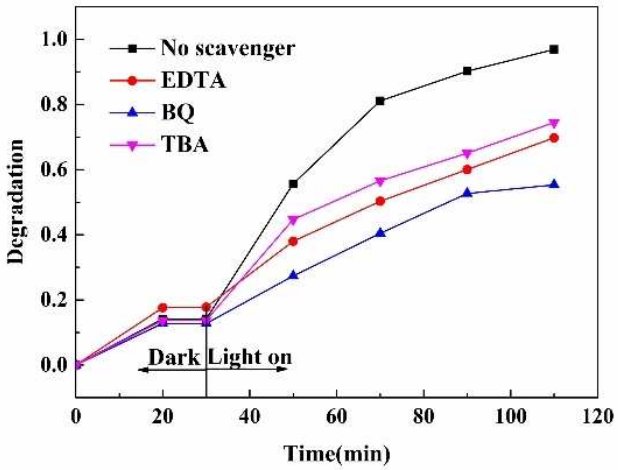

Figure 10. Photocatalytic degradation of RhB over BO-BV3 under different conditions with exposure to visible light: original, adding EDTA, adding BQ, and adding TBA.

$$\text{BO-BV3} + h\nu \rightarrow \text{BO-BV3}(+eCB^-) \quad (3)$$

$$eCB^- + O_2 \rightarrow O_2\bullet^- \quad (4)$$

$$hVB^+ + H_2O \rightarrow H^+ + \bullet OH \quad (5)$$

$$O2\bullet^- + H^+ \rightarrow \bullet H2O \quad (6)$$

$$eCB^- + \bullet H2O + H+ \rightarrow H_2O_2 \quad (7)$$

$$H_2O_2 \rightarrow 2\ \bullet OH \quad (8)$$

$$RhB^+ \text{ active species}(O2\bullet^-, hVB^+, \bullet OH) \rightarrow \text{degraded products} \quad (9)$$

Conclusions

$BiVO_4/\alpha$, β-Bi_2O_3 heterostructures were successfully fabricated by electrospinning with a hydrothermal process. The results show that the addition of $BiVO_4$ has a great effect on the formation of β-Bi_2O_3 and the structure of the nanofibers, which are crucial for the photocatalytic performance of the samples. The formation process of the as-prepared nanofibers can be divided into two steps: the oxidation and decomposition of precursor nanofibers (heating) and the crystallization and growth of α, β-Bi_2O_3 (cooling). Compared to pure $BiVO_4$ and Bi_2O_3, the $BiVO_4/\alpha$, β-Bi_2O_3 nanofiber nanocomposites exhibited better photocatalytic behavior for the decomposition of RhB and Tc. The improved photocatalytic activity of the as-prepared nanocomposites may originate from the increased light absorption and separation of photogenerated carriers, which is derived from the addition of $BiVO_4$. Furthermore, the sample with a $BiVO_4$ content of 3 wt% displayed the best photocatalytic activity on RhB compared to that of the other samples analyzed in this study. The reactive species in the photocatalytic process were deduced to be as follows: $O_2\bullet^- > h^+ >$ •OH.

Supporting Information Summary

Experimental procedures are available in supporting information.

Acknowledgement

This work was supported by the National Science Foundation of China (Nos. 21576220 and 21276208), the Natural Science Foundation of Shaanxi Province (No. 2015JZ005) and the Key Laboratory Research Project of Shaanxi Province (No. 17JS085).

Conflict of Interest

The authors declare no conflict of interest.

Keywords: $BiVO_4/\alpha$ · β-Bi_2O_3 · electrospinning · nanofibers · photocatalytic

[1] a) Y. h. Lv, W. Q. Yao, R. L. Zong, Y. F. Zhu, *Sci. Rep.* **2016**, *6*, 19347; b) A. Baral, D. P. Das, M. Minakshi, M. K. Ghosh, D. K. Padhi, *Chemistry- Select* **2016**, *14*, 4277–4285.
[2] a) O. H. Hicham, S. Rakassa, F. T. Al Wadaani. J. Taibah Univ, *Sci.* **2015**, *9*, 508–512; b) X. F. Chen, J. F. Dai, G. F. Shi, H. Yang, *Ultrason. Sonochem.* **2016**, *29*, 172–177; c) J. Zhang, Q. F. Han, X. Wang, J. W. Zhu, G. R. Duan, *Mater. Lett.* **2016**, *162*, 218–221.
[3] a) L. L. Yang, Q. F. Han, J. Zhao, J. W. Zhu, X. Wang, W. H. Ma, *J. Alloys Compd.* **2016**, *614*, 353–359; b) Y. Lu, Y. Zhao, J. Z. Zhao, Y. H. Song, Z. F. Huang, F. F. Gao, N. Li, Y. W. Li, *Ceram. Int.* **2016**, *42*, 4779–4787; c) S. Sood, A. Umar, S. K. Mehta, S. K. Kansal, *Ceram. Int.* **2015**, *41*, 3355–3364.
[4] D. Sánchez-Martínezn, I. Juárez-Ramírez, L. M. Torres-Martínez, *Ceram. Int.* **2016**, *42*, 2013–2020.
[5] Z. h. Ai, Y. Huang, S. C. Lee, L. Z. Zhang, *J. Alloys Compd.* **2011**, *509*, 2044–2049.
[6] X. C. Luo, G. Q. Zhu, J. H. Peng, X. M. Wei, M. Hojamberdiev, L. Jin, P. Liu, *Appl. Surf. Sci.* **2015**, *351*, 260–269.
[7] H. F. Cheng, B. B. Huang, J. B. Lu, Z. Y. Wang, B. Xu, X. Y. Zhang, Y. Dai, *Phys. Chem. Chem. Phys.* **2010**, *12*, 15468–15475.
[8] D. F. Yu, F. Teng, L. Q. Yang, L. Pang, Q. Xu, Q. Q. Zhang, *ChemistrySelect* **2016**, *1*, 4209–4217.
[9] X. Liu, Y. Kang, *Mater. Lett.* **2016**, *164*, 229–231.
[10] S. Sood, S. K. Mehta, A. S. K. Sinha, S. KumarKansal, *Chem. Eng. J.* **2016**, *290*, 45–52.
[11] a) Y. Q. Cong, Y. Ji, Y. H. Ge, H. Jin, Y. Zhang, Q. Wang, *Chem. Eng. J.* **2017**, *307*, 572–582; b) L. W. Shan, G. L. Wang, L. Z. Liu, Z. Wu, *J. Mol. Catal. A: Chem.* **2015**, *406*, 145–151.
[12] H. N. Che, J. B. Chen, K. Huang, W. Hu, H. Hu, X. T. Liu, G. B. Che, C. B. Liu, W. D. Shi, *J. Alloys Compd.* **2016**, *688*, 882–890.
[13] A. Ren, C. B. Liu, Y. Z. Hong, W. D. Shi, S. Lin, P. Li, *Chem. Eng. J.* **2014**, *258*, 301–308.
[14] X. Liu, Y. Kang, D. Luo, *Mater. Lett.* **2016**, *185*, 189–192.
[15] S. Balachandran, M. Swaminathan, *J. Phys. Chem. C* **2012**, *116*, 26306–26312.
[16] Y. C. Huang, W. J. Fan, B. Long, H. B. Li, F. Y. Zhao, Z. L. Liu, Y. X. Tong, H. B. Ji, *Appl. Catal. B: Environ.* **2016**, *185*, 68–76.
[17] Y. Y. Shi, L. J. Luo, Y. F. Zhang, Y. Chen, S. Wang, L. X. Li, Y. J. Long, F. Z. Jiang, *Ceram. Int.* **2017**, *43*, 7627–7635.
[18] a) A. S. Manjunatha, N. S. Pavithra, S. Marappa, S. A. Prashanth, G. Nagaraju, Puttaswamy, *ChemistrySelect* **2018**, *47*, 13456–13463; b) Y. S. Fu, X. Q. Sun, X. Wang, *Mater. Chem. Phys.* **2011**, *131*, 325–330.
[19] M. M. Mao, F. Chen, C. C. Zheng, J. Q. Ning, Y. J. Zhong, Y. Hua, *J. Alloys Compd.* **2016**, *688*, 1080–1087.
[20] L. Z. Li, B. Yan, *J. Alloys Compd.* **2009**, *476*, 624–628.
[21] R. S. Ganesha, S. K. Sharmab, E. Durgadevic, M. Navaneethan, S. Ponnusamy, C. Muthamizhchelvan, Y. Hayakawa, D. Y. Kim, *Mater. Res. Bull.* **2017**, *94*, 190–198.
[22] M. Bagheri, M. Heydari, M. R. Vaezi, *J. Phys. Chem. Solids* **2018**, *112*,14–19.
[23] S. Mohan, B. Sivakumar, R. V. Kulangara, B. Subramanian, *Chemistry-Select* **2016**, *1*, 6961–6971.
[24] H. Lim, S. B. Rawal, Prog, *Nat. Sci.: Mater.* **2017**, *27*, 289–296.
[25] Z. M. Zhang, N. W. L. H. Zhu, H. Q. Lv, *J. Enviro. Chem. Eng.* **2017**, *5*, 915–923.
[26] Z. L. Yang, J. Lu, W. C. Ye, C. S. Yu, Y. L. Chang, *Appl. Surf. Sci.* **2017**, *392*, 472–480.
[27] L. J. Cheng, Y. Kang, *J. Alloys Compd.* **2014**, *585*, 85–93.
[28] S. Sarkar, K. K. Chattopadhyay, *Physica E* **2014**, *58*, 52–58.
[29] Y. Y. Zhang, Y. P. Guo, B. J. Fang, Y. J. Chen, H. N. Duan, H. Li, H. Z. Liu, *Appl. Catal. A: Gen.* **2016**, *514*, 146–153.
[30] X. N. Liu, Q. F. Lu, C. Q. Wang, *Mater. Lett.* **2015**, *154*, 81–84.
[31] M. Wang, Z. L. Liu, M. H. Fang, C. Tang, Z. H. Huang, Y. G. Liu, X. W. Wu, Y. J. Mao, *Solid State Sci.* **2016**, *55*, 1–7.
[32] M. X. Zhang, P. M. Kelly, M. A. Easton, J. A. Taylora, *Acta Mater.* **2005**, *53*, 1427–1438.
[33] J. G. Lv, Q. Q. Zhu, Z. Zeng, M. Zhang, J. Yang, M. Zhao, W. H. Wang, Y. B. Cheng, G. He, *J. Phys. Chem. Solids* **2017**, *111*, 104–109.
[34] S. W. Liu, K. Yin, W. S. Ren, B. Cheng, J. G. Yu, *J. Mater. Chem.* **2012**, *22*, 17759–17767.
[35] W. L. Shi, F. Guo, S. L. Yuan, *Appl. Catal. B: Environ.* **2017**, *209*, 720–728.
[36] a) Q. Y. Li, Z. Y Zhao, *Phys. Lett. A* **2015**, *379*, 2766–2771; b) J. J. Sun, X. Y. Li, Q. D. Zhao, M. O. Tadé, S. M. Liu, *Appl. Catal B: Environ.* **2017**, *219*, 259–268.
[37] K. Wangkawong, S. Phanichphant, D. Tantraviwat, B. Inceesungvorn, *J. Colloid Interface Sci.* **2015**, *454*, 210–215.
[38] J. Chen, D. Z. Li, J. B. Wang, P. Wang, C. S. Cao, Y. Shao, J. X. Wang, J. J. Xian, *Appl. Catal. B: Environ.* **2015**, *163*, 323–329.

Submitted: February 15, 2019
Accepted: July 17, 2019